Proceedings of the Jangjeon Mathematical Society
29 (2026), No. 2, pp. 443 - 472

www.jangjeon.or.kr
http://dx.doi.org/10.17777/pjms2026.29.2.020

ELECTROOSMOTIC-DRIVEN PERISTALTIC TRANSPORT OF NANOFLUIDS IN A VERTICAL POROUS CHANNEL WITH ROUGH WALLS

BHAVANA GADAD[1], **JYOTI SHETTY**[1], **RAJASHEKHAR CHOUDHARI**[1,*],
HANUMESH VAIDYA[2], **BALACHANDRA HADIMANI**[3], AND **K. V. PRASAD**[2]

Abstract. The electroosmotic peristaltic transport of nanofluids in a rough vertical channel is explored. The flow is subjected to a transverse magnetic field with particular focus on the electroosmotic effects caused by an applied electric field along the axis of the channel. The model includes second-order velocity slip and thermal slip boundary conditions to precisely capture microfluidic behavior in the vicinity of the wall. The channel walls have surface roughness that interacts with peristaltic wave motion and the electroosmotic body force, highly altering the structure of the flow. The nanofluids improves the thermal properties, leading to enhanced heat transfer efficiency. The nonlinear governing equations are obtained under long-wavelength and low-Reynolds-number assumptions and are solved through the Homotopy Perturbation Method (HPM) using Mathematica. It is observed that the electroosmotic parameter dominates the regulation of flow velocity, temperature field, and pressure distribution. The analysis shows that strengthening the electroosmotic increases flow and decreases trapping, while slip conditions and wall roughness offer efficient control of heat and fluid transport. This paper provides useful insights for the optimisation of electrokinetically driven microfluidic devices, such as lab-on-a-chip devices, drug delivery devices, and bio-microelectromechanical systems (Bio-MEMS).

Keywords and phrases. Electroosmotic Flow, Homotopy Perturbation Method, Roughness, Second Order Velocity Slip.

1. Introduction

Nanoscale and microscale fluid transport plays a pivotal role in the operation of microfluidic and nanofluidic devices and has broader implications for biomedical as well as engineering applications. At such microscopic levels, the classical fluid dynamics are affected by common physical effects like surface forces, electrokinetic effects, and enhanced heat and mass transfer by the presence of nanoparticles and electric fields. Several mechanisms drive flow at such scales, and peristalsis plays an important role by enabling fluid transport through wave-like wall contractions and channel relaxations. The mechanism is specifically useful in flexible conduits and is employed in the design of effective microfluidic pumping systems where mechanical elements are either limited or undesirable. Peristalsis, wave-type muscular contraction traveling along a compliant tube, is a fundamental mechanism through which biological systems achieve directional transport of suspensions and fluids. It governs a wide array of important functions in the human body, such as blood flow in arteries and veins, chyme movement along the gastrointestinal tract, flow of urine along the ureters, and sperm movement along the reproductive tract [1] [2] [3]. The flows do not occur in idealized geometries but in tubes that are perhaps asymmetric, vertically placed, or implanted in porous tissues [4] [5]. Such structural complexity influences peristaltic motion behavior, leading to phenomena such as flow reversal, asymmetry in velocity, and altered pressure gradients, all of which are intrinsic to the physiological function of the system. The ability of peristalsis to achieve efficient, low-shear transport is optimally suited to the preservation of the integrity of shear-sensitive biological material and therefore finds itself an integral component of processes involving gentle manipulation of living cells or macromolecules [6]. The benefits of peristalsis reach far beyond physiology. Peristaltic action is used extensively in fluid flow systems engineering, where sterility, isolation, and accuracy are required [7]. Peristaltic action pumps can move corrosive, viscous, or particulate-containing fluids without subjecting them to mechanical parts, thus avoiding contamination and degradation. The method becomes especially valuable in drug delivery systems, chemical reactors, food, and pharmaceutical processing streams [8] [9].

In addition, the allure of geometrical and material complexities has major implications for the performance of the peristaltic systems. Channels are asymmetric, which changes velocity and pressure distributions, vertical or inclined orientations have a gravitational force effect, and porous media establish flow regulation by means of permeability and porosity [10]. Such characteristics are common in both natural tissues and industrial environments, and they can influence the dynamics of peristaltic flow and provide avenues for controlling the flow's behaviour. The bigger strengths of the peristaltic systems, including their ability to accelerate heat and mass transfer, as well as maintain transport in the absence of a favourable pressure gradient, have encouraged additional theoretical and applied research efforts on the benefits of these systems in science and research [11]. The electroosmotic forces and nanofluids both comprises an effective base to micro and nano fluidic systems. The physical phenomenon of electroosmotic flow (EOF) presents a beautiful, non-mechanical method of driving fluids through the interaction of applied electric fields and surface charge. Applying an electric field across an electrolyte near a charged surface will mobilize the electrical double layer and cause an electrical breakthrough without the requirement of moving components [12] [13]. Electroosmotic velocity is linear with applied field strength, which means very accurate control over the transport regime, and a vast amplification of the movement of ions and water is possible. In addition, the channel geometry and asymmetry of surface charge provide additional control of the directionality of flow and rectification, which is especially useful in the case of nano fluidics, where the manipulation of fluid is crucial [14] [15]. Comparable to EOF, nanofluids, which are fluids that contain metallic or hybrid nanoparticles, improve the transport behaviour significantly. These fluids have high thermo-conduction and increased heat transfer, which is imperative in sustaining thermo stability and efficiency in constricted microchannels [16] [17], as exhibited by the conventional fluids. In applications where a high rate of delivery of molecules or mixing is needed, nanofluids have been found to facilitate mass transport by increasing fluid velocity and mixing beyond what is obtainable by using conventional fluids. The electroosmotic and peristaltic flows of nanofluids have been studied immensely by taking into consideration the magnetic fields, the porous media, wall roughness, and slip conditions factors. Nevertheless, although there has been some advancement in the modeling of these effects either as individual effects or interacting with one another, there has not been a framework for all four of them. The results of the impacts of magnetic fields are commonly investigated in microfluidics model where, in many cases, their inhibitory effect on the flow is observed [18]. Riaz et al. [19] numerically investigated the peristaltic flow of a Jeffrey nanofluid in an asymmetric porous channel in the presence of an applied magnetic field and recorded a decrease in velocity owing to Lorentz forces, in a similar work that analytically analyses the electrokinetic flow of a nanofluid in a homogeneous and isotropic porous microtube with a transverse magnetic field, Reza and Rana [20] present comparable magnetic resistance to transport. These two studies, however, assumed that the walls were smooth without the inclusion of higher-order slip formulations. The porous media have been included in the Darcy-Brinkman formations. Abouzeid and Shaaban [21] simulated the electroosmotic flow of non-Newtonian non-Darcy nanofluid in a porous medium and managed to relate the thermal gradients to the porous resistance. It has also been revealed that wall roughness also affects microflow dynamics. Srinivas and Gayathri [22], studies the porous peristaltic wave with the vertical channel emphasizing the realistic way of studying biomicrofluidics, Wang and Kang [23] showed through numerical simulation that surface roughness when random in nature changes electroosmotic velocity profiles significantly. Vaidya et al. [24] extended the study of MHD peristaltic flow of a Casson nanofluid in a geometrically rough channel with slip at the wall and demonstrated that roughness increases by elevating the resistance to flow and altering the bolus configurations. These models, however, did not take into consideration porous drag or second-order slip. Slip conditions, especially for the second order, remain underexplored. Kundu and Saha [25] noted that second-order velocity and thermal slip can strongly influence microscale transport, yet few models integrate such conditions with MHD, porosity, or roughness. To overcome the nonlinear character of the governing equations, the Homotopy Perturbation Method (HPM), as developed by He [26], is used for its efficiency in solving complicated boundary value problems to a high degree of accuracy. Although there have been a lot of studies [27], there are fewer studies on semi-analytical models that would be simultaneously affected by the magnetic fields, porous media, roughness of the walls, and second-order velocity and thermal slip in peristaltic nanofluidic transport or electroosmotic transport of nanofluids. There are some studies that show such effects in isolation or only in combination. This creates a gap in the representation of the ideal microfluidic settings in the real world. This gap is filled in the current work and is characterized by a comprehensive analytical approach describing all four coupled mechanisms [28] [29] [30]. This study seeks to develop a semi-analytical model that considers the interactive effects of a magnetic field, porous medium, wall roughness, and second-order velocity and thermal slip on nanofluid transport under the action of electroosmotic and peristaltic movements. By formulating the governing equations of the intricate physical setup, the work explores how each parameter influences flow dynamics, heat transfer, and mass transport. The very nonlinear system is resolved by the use of the Homotopy Perturbation Method (HPM) to achieve an approximate analytical solution. This method allows in-depth analysis of microscale interactions with direct application to biomedical devices, micro-pumps, and lab-on-chip technologies. A primary distinguishing characteristic of this work is its complete unification of all these microfluidic effects into one analytical framework in contrast to earlier studies that primarily examine isolated or partially coupled phenomena. The findings provide new theoretical explanations of how multi-physics interactions control transport efficiency, and flow control in realistic microfluidic environments.

2. Mathematical Formumation

A tapered asymmetric geometry with rough walls is considered for the flow analysis. The flow of an incompressible nanofluid is examined along the axial and transverse directions, denoted by $\overline{X}$ and $\overline{Y}$, respectively, as illustrated in Fig. 1. The corresponding velocity components in these directions are represented by $\overline{U}$ (axial) and $\overline{V}$ (transverse). The fluid is subjected to a magnetic field, an electroosmotic force, and slip parameters which greatly affect the geometry. The upper and lower walls are asymmetric and undergo peristaltic wave motion with different amplitudes a_1 and b_1. The flow is driven by a combination of electroosmotic body force, pressure gradient, and peristaltic motion in the axial direction x, with transverse coordinate y. The deformation of the peristaltic channel wall is expressed as follows.

$$H_1 = d_1 + \cos\left(\frac{2\pi}{\lambda}(\bar{X} - c\bar{t})\right) - \phi_2 \cos^4\left(\frac{\pi\bar{X}}{\lambda_1}\right), \tag{1}$$

$$H_2 = d_2 + \cos\left(\frac{2\pi}{\lambda}(\bar{X} - c\bar{t}) + \phi_1\right) - \phi_2 \cos^4\left(\frac{\pi\bar{X}}{\lambda_1}\right). \tag{2}$$

Where $d_1 + d_2$ is the width of the channel, a_1 and b_1 are the amplitudes of the left and right walls, λ is the wavelength, ϕ_1 is the phase difference, where $0 \leq \phi_1 \leq \pi$ and $a_1^2 + b_1^2 + 2a_1 b_1 \cos\phi_1 \leq (d_1 + d_2)^2$, where this condition is satisfied by the a_1, b_1, d_1, d_2 and ϕ_1. Constant Pressure difference is assumed across the boundaries of the channel, and the For electroosmotic-

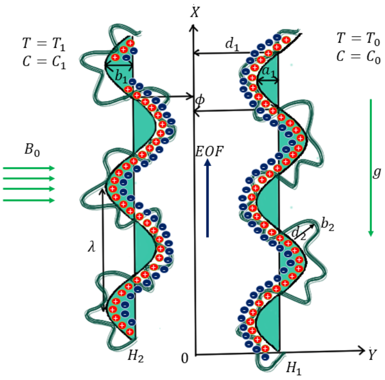

Figure 1. Schematic of a two-dimensional vertical porous channel with rough walls undergoing electroosmotic-driven peristaltic transport.

driven peristaltic transport of nanofluids in a vertical porous channel with rough walls under a magnetic field, the continuity, momentum, energy, and concentration equations are modelled accordingly.

$$\frac{\partial \overline{U}}{\partial \overline{X}} + \frac{\partial \overline{V}}{\partial \overline{Y}} = 0, \tag{3}$$

$$\begin{aligned}\rho_f\left(\frac{\partial \overline{U}}{\partial \overline{t}} + \overline{U}\frac{\partial \overline{U}}{\partial \overline{X}} + \overline{V}\frac{\partial \overline{U}}{\partial \overline{Y}}\right) = -\frac{\partial \overline{P}}{\partial \overline{X}} + \mu\left(\frac{\partial^2 \overline{U}}{\partial \overline{X}^2} + \frac{\partial^2 \overline{U}}{\partial \overline{Y}^2}\right) - \frac{\mu_f}{k_1}\overline{U} - \sigma B_0^2 \overline{U} + \rho_e E_x \\ + (1-C_0)\rho_f g\beta(T-T_0) + (\rho_p-\rho_f)g\beta(C-C_0),\end{aligned} \tag{4}$$

$$\rho_f\left(\frac{\partial \overline{V}}{\partial \overline{t}} + \overline{U}\frac{\partial \overline{V}}{\partial \overline{X}} + \overline{V}\frac{\partial \overline{V}}{\partial \overline{Y}}\right) = -\frac{\partial \overline{P}}{\partial \overline{Y}} + \mu_f\left(\frac{\partial^2 \overline{V}}{\partial \overline{X}^2} + \frac{\partial^2 \overline{V}}{\partial \overline{Y}^2}\right), \tag{5}$$

$$\begin{aligned}\rho_f c_f\left(\frac{\partial \overline{T}}{\partial \overline{t}} + \overline{U}\frac{\partial \overline{T}}{\partial \overline{X}} + \overline{V}\frac{\partial \overline{T}}{\partial \overline{Y}}\right) = k\left(\frac{\partial^2 \overline{T}}{\partial \overline{X}^2} + \frac{\partial^2 \overline{T}}{\partial \overline{Y}^2}\right) \quad + \rho c_f\left[D_B\left(\frac{\partial \overline{C}}{\partial \overline{X}}\frac{\partial \overline{T}}{\partial \overline{X}} + \frac{\partial \overline{C}}{\partial \overline{Y}}\frac{\partial \overline{T}}{\partial \overline{Y}}\right)\right. \\ \left. + \frac{D_T}{T_0}\left(\left(\frac{\partial \overline{T}}{\partial \overline{X}}\right)^2 + \left(\frac{\partial \overline{T}}{\partial \overline{Y}}\right)^2\right)\right] \quad + \sigma B_0^2 \overline{U}^2,\end{aligned} \tag{6}$$

$$\frac{\partial \overline{C}}{\partial \overline{t}} + \overline{U}\frac{\partial \overline{C}}{\partial \overline{X}} + \overline{V}\frac{\partial \overline{C}}{\partial \overline{Y}} = D_B\left(\frac{\partial^2 \overline{C}}{\partial \overline{X}^2} + \frac{\partial^2 \overline{C}}{\partial \overline{Y}^2}\right) + \frac{D_T}{T_0}\left(\frac{\partial^2 \overline{T}}{\partial \overline{X}^2} + \frac{\partial^2 \overline{T}}{\partial \overline{Y}^2}\right). \tag{7}$$

The steady frames are replaced with moving reference wave frames with the velocity c. Because the motion is steady in wave frames $(\bar{x}, \bar{y})$ but unsteady in fixed frames $(\bar{X}, \bar{Y})$, the relationship between the wave and fixed frames is given below,

$$(8)\quad \bar{v} = \bar{V}, \quad \bar{u} = \bar{U} - c, \quad \bar{y} = \bar{Y}, \quad \bar{x} = \bar{X} - c\bar{t}, \quad p(\bar{x},\bar{y}) = \bar{P}(\bar{X},\bar{Y},\bar{t}),$$
$$T(\bar{x},\bar{y}) = \bar{T}(\bar{X},\bar{Y},\bar{t}), \quad C(\bar{x},\bar{y}) = \bar{C}(\bar{X},\bar{Y},\bar{t}).$$

A uniform transverse magnetic field B_0 is imposed along the y-axis. By applying Ohm's law, the resulting Lorentz force term that accounts for the MHD effect in the flow dynamics is obtained as:

$$(9)\qquad \bar{\mathbf{J}} \times \bar{\mathbf{B}} = \begin{bmatrix} -\sigma_e B_0^2 \bar{U} \\ 0 \\ 0 \end{bmatrix}.$$

The Poisson–Boltzmann distribution is the basic model used to describe the electrical potential variation in microchannels, particularly due to the presence of an electric double layer (EDL) near the charged surfaces. This distribution arises from the interaction between electrostatic forces and the thermal motion of ions in the electrolyte. It is developed by combining the Poisson equation, which relates the electric potential to the charge density, and the Boltzmann distribution, which describes how ion concentration varies with the electric potential:

$$\nabla^2 \bar{E} = -\frac{\rho_e}{\varepsilon_0 \varepsilon_r}, and \rho_e = ez(n^+ - n^-).$$

The model assumes that ions are thermally excited and that their concentrations follow an exponential relationship with the local electric potential, given by:

$$n^{\pm} = n_0 \exp\left(\frac{-ez\bar{E}}{k_B T}\right).$$

In conditions of low surface potential and negligible EDL overlap, the governing equations simplify, allowing analytical solutions in many practical cases. This distribution is widely used in electrokinetic flow analysis and aids in understanding the behavior of ions and potentially harmful substances in the bloodstream.

The current model is constructed under the assumptions of long wavelength and low Reynolds number. Moreover, body forces like gravity and complex effects such as viscoelasticity, non-uniform surface charge, or Joule heating are excluded to ensure analytical tractability. While these assumptions are standard in electroosmotic and peristaltic microflows, they may limit applicability in high-speed, large-scale, or highly non-Newtonian regimes. Now, by imposing the non-dimensional parameters and variables,

$$(10)\quad x = \frac{\overline{x}}{\lambda}, \; y = \frac{\overline{y}}{d_1}, \; u = \frac{\overline{u}}{c}, \; v = \frac{\overline{v}}{c\delta}, \; \delta = \frac{d_1}{\lambda}, \; p = \frac{\overline{p}\, d_1^2}{\mu_f \lambda c}, \; \mathrm{Re} = \frac{d_1 c}{\vartheta}, \; \vartheta_f = \frac{\mu_f}{\rho_f},$$

$$N_b = \frac{\tau D_B (C_1 - C_0)}{\vartheta_f}, \; N_t = \frac{\tau D_T (T_1 - T_0)}{T_0 \vartheta_f}, \; \theta = \frac{T - T_0}{T_1 - T_0}, \; \sigma = \frac{C - C_0}{C_1 - C_0}, \; t = \frac{\overline{t}c}{\lambda},$$

$$a = \frac{a_1}{d_1}, \; b = \frac{b_1}{d_1}, \; d = \frac{d_2}{d_1}, \; h_1 = \frac{H_1}{d_1}, \; h_2 = \frac{H_2}{d_1}, \; \kappa = \frac{k_1}{d_1^2}, \; M = B_0 d_1 \sqrt{\frac{\sigma_e}{\mu_f}},$$

$$U_{hs}=\frac{d_1^2E\varepsilon\zeta}{\mu_f c},\ E=\frac{\overline{E}}{\zeta},\ \phi_2=\frac{a_2}{d_1},\ G_c=\frac{(\rho_p-\rho_f)g\beta_c d_1^2(C_1-C_0)}{c\mu_f},$$
$$G_r=\frac{(1-C_0)\rho_f g\beta_c d_1^2(T_1-T_0)}{c\mu_f},\ P=-\frac{dp}{dx},\ \tau=\frac{(\rho C')_p}{(\rho C')_f}.$$

By employing the non-dimensional parameters and variables, and by assuming the long wavelength ($\delta \ll 1$) and low Reynolds number approximations ($\mathrm{Re} \ll 1$), we obtain the following equations:

$$-\frac{\partial p}{\partial x}+\frac{\partial^2 u}{\partial y^2}-\frac{1}{\kappa}(u+1)+G_r\theta+G_c\sigma+m_e^2U_{hs}E-M^2(u+1)=0, \tag{11}$$

$$-\frac{\partial p}{\partial y}=0, \tag{12}$$

$$\frac{\partial^2\theta}{\partial y^2}+N_b\frac{\partial\theta}{\partial y}\frac{\partial\sigma}{\partial y}+N_t\left(\frac{\partial\theta}{\partial y}\right)^2+M^2(u+1)^2=0, \tag{13}$$

$$\frac{\partial^2\sigma}{\partial y^2}+\frac{N_t}{N_b}\frac{\partial^2\theta}{\partial y^2}=0. \tag{14}$$

The dimensionless boundary conditions are given below, as the second-order velocity slip and first-order thermal and concentration slip are introduced. In this context, $h_1(x)$ and $h_2(x)$ denote the dimensionless shapes of the upper and lower peristaltic walls, respectively, given by:

$$u=-1-\beta_1\frac{\partial u}{\partial y}-\beta_2\frac{\partial^2 u}{\partial y^2},\quad \theta+\beta_3\frac{\partial\theta}{\partial y}=0,\quad \sigma+\beta_4\frac{\partial\sigma}{\partial y}=0, \tag{15}$$
$$\text{at } h_1(x)=1+a\cos(2\pi x)-\phi_2\cos^4\left(\frac{\pi x}{\lambda_1}\right).$$

$$u=-1+\beta_1\frac{\partial u}{\partial y}+\beta_2\frac{\partial^2 u}{\partial y^2},\quad \theta-\beta_3\frac{\partial\theta}{\partial y}=0,\quad \sigma-\beta_4\frac{\partial\sigma}{\partial y}=0, \tag{16}$$
$$\text{at } h_2(x)=-d-b\cos(2\pi x+\phi_1)-\phi_2\cos^4\left(\frac{\pi x}{\lambda_1}\right).$$

Eq. (12) indicates that the pressure p is independent of the transverse coordinate y. In the laboratory frame, the dimensional volumetric flow rate is given by:

$$Q=\int_{H_2(X,t)}^{H_1(X,t)}U(X,Y,t)\,dY. \tag{17}$$

Where H_1 and H_2 are functions of both the axial coordinate X and time t. When transformed into the wave frame, the expression becomes:

$$q=\int_{h_2(x)}^{h_1(x)}u(x,y)\,dy. \tag{18}$$

Here, $h_1(x)$ and $h_2(x)$ represent the shapes of the upper and lower channel walls in the wave frame and depend solely on x. From Eq. (8), (17), and (18), the relationship between flow rates in the laboratory and wave frames can be expressed as:

$$Q = q + ch_1(x) - ch_2(x). \tag{19}$$

The time-averaged volumetric flow rate over a complete period T, at a fixed axial location X, is given by:

$$\bar{Q} = \frac{1}{T}\int_0^T Q\,dt. \tag{20}$$

Substituting Eq. (19) into Eq. (20) and performing the integration, we obtain:

$$\bar{Q} = q + cd_1 + d_2. \tag{21}$$

If we define the dimensionless flow rate in the laboratory and wave frames as:

$$\Theta = \frac{\bar{Q}}{cd_1}, \quad F = \frac{q}{cd_1}. \tag{22}$$

Then Eq. (21) simplifies to:

$$\Theta = F + 1 + d. \tag{23}$$

Here, $d = d_1 + d_2$ represents the total average width of the asymmetric channel, where

$$F = \int_{h_2}^{h_1} u\,dy. \tag{24}$$

Using Eq. (11) and (24), the pressure gradient $\frac{\partial p}{\partial x}$ is calculated. The non-dimensional pressure rise per wavelength is given by:

$$\Delta P = \int_0^1 \frac{\partial p}{\partial x}\,dx. \tag{25}$$

3. METHODOLOGY

The solution has been obtained by the Homotopy Perturbation Method (HPM). He [26] initially presented the novel Homotopy Perturbation Method (HPM) as a reliable approach for resolving both differential and integral problems. In contrast to traditional perturbation techniques, HPM integrates elements of topology through the concept of homotopy. In this methodology, a homotopy function is represented as:

$$\hat{h}(\hat{x},\hat{q}) : \Omega \times [0,1] \rightarrow \mathbb{R}$$

, wherein the analysis treats $\hat{q} \in [0,1]$ as a small parameter, acting as an embedding parameter. Notably, HPM stands out for its exceptional ability to achieve rapid convergence without requiring a naturally small parameter within the governing equation. The following are the homotopies for velocity, temperature, and concentration profiles in HPM, obtained by applying the method to Eq. (11) to (14), respectively:

(26)

$$\hat{h}(u,\hat{q}) = (1-\hat{q})\left[\hat{L}(u) - \hat{L}(u_0)\right] + \hat{q}\left[\hat{L}(u) - \frac{1}{\kappa}(u+1) + G_r\theta + G_c\sigma + m_e^2 U_{hs} E - M^2(u+1)\right],$$

(27)

$$\hat{h}(\theta,\hat{q}) = (1-\hat{q})\left[\hat{L}(\theta) - \hat{L}(\theta_0)\right] + \hat{q}\left[\hat{L}(\theta) + N_b\frac{\partial\theta}{\partial y}\frac{\partial\sigma}{\partial y} + N_t\left(\frac{\partial\theta}{\partial y}\right)^2 + M^2(u+1)^2\right],$$

$$\hat{h}(\sigma,\hat{q}) = (1-\hat{q})\left[\hat{L}(\sigma) - \hat{L}(\sigma_0)\right] + \hat{q}\left[\hat{L}(\sigma) + \frac{N_t}{N_b}\frac{\partial^2\theta}{\partial y^2}\right]. \tag{28}$$

For convenience, we choose the linear operator $\hat{L} = \frac{\partial^2}{\partial y^2}$. The following series expansions are constructed to obtain a complete solution:

$$u(x,y) = u_0 + \hat{q}u_1 + \hat{q}^2u_2 + \cdots \tag{29}$$

$$\theta(x,y) = \theta_0 + \hat{q}\theta_1 + \hat{q}^2\theta_2 + \cdots \tag{30}$$

$$\sigma(x,y) = \sigma_0 + \hat{q}\sigma_1 + \hat{q}^2\sigma_2 + \cdots \tag{31}$$

In *Mathematica*, series solutions for the velocity $u(y)$, temperature $\theta(y)$, and concentration $\sigma(y)$ were derived by expressing each variable as a power series in terms of the embedding parameter $\hat{q}$, and substituting them into the governing nonlinear ordinary differential equations (ODEs). The coefficients of the series were calculated using recurrence relations by matching like powers of $\hat{q}$. The associated boundary conditions were applied symbolically to determine the unknown constants in each order of approximation. The series were truncated after including a sufficient number of terms to ensure convergence and computational accuracy. This symbolic technique provided a robust and precise approach for solving the highly coupled, nonlinear system of equations.

4. VALIDATION OF RESULTS

To validate our findings, we have limited values of particular parameters and performed comparative analysis with homotopy perturbation solutions. In the absence of nanofluid, electroosmosis, and a magnetic field, the current model is validated. The current model is visualized and compared with the findings of [22]. Fig. 2 demonstrates a strong agreement between the present results and those reported by [22], thereby reinforcing the validity of the current model and its predictions. The slight variation can be observed due to the inclusion of additional parameters, magnetic field, electroosmotic flow which appear in the denominator and prevent it from reducing exactly to zero, unlike the reference model.”

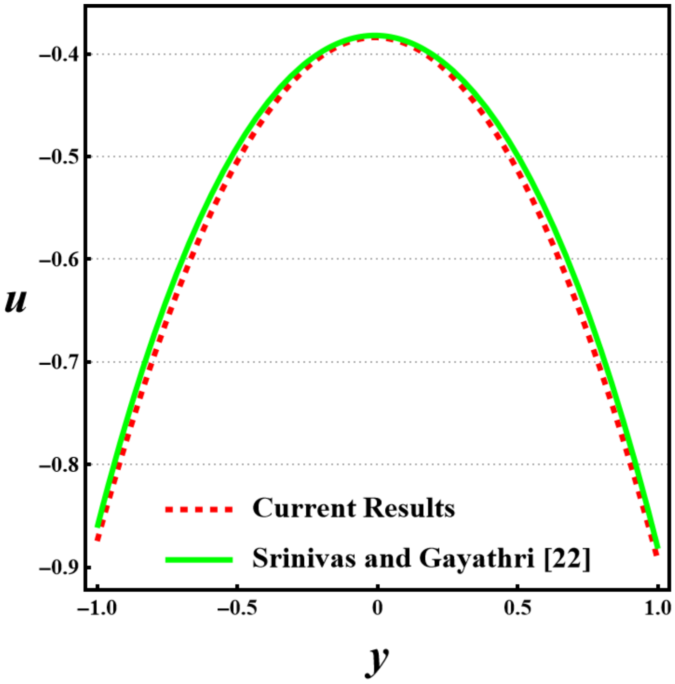

Figure 2. Validation of the present model velocity profile with the HPM solution [22].

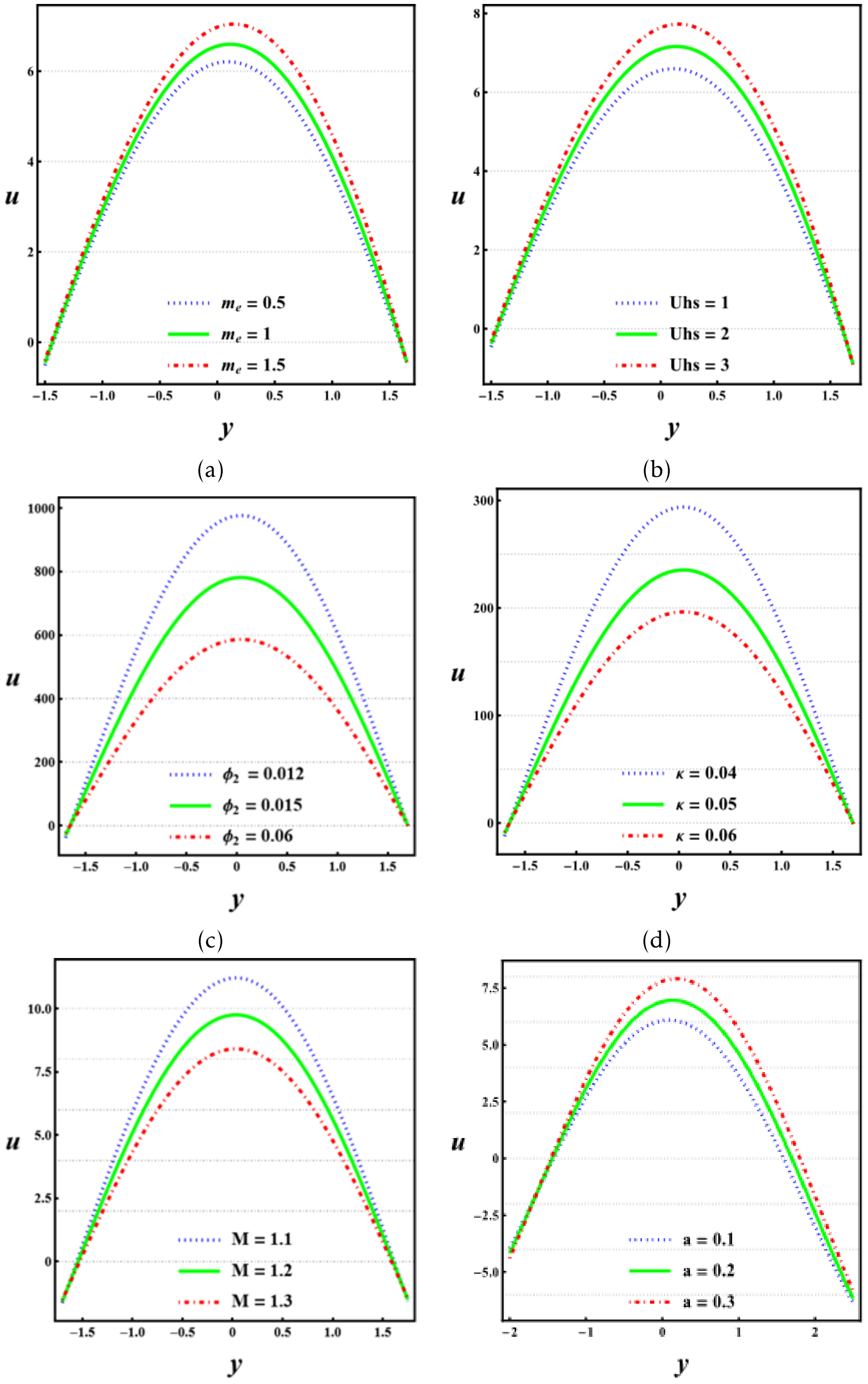
u
y
$m_e = 0.5$
$m_e = 1$
$m_e = 1.5$
Uhs = 1
Uhs = 2
Uhs = 3
$\phi_2 = 0.012$
$\phi_2 = 0.015$
$\phi_2 = 0.06$
$\kappa = 0.04$
$\kappa = 0.05$
$\kappa = 0.06$
M = 1.1
M = 1.2
M = 1.3
a = 0.1
a = 0.2
a = 0.3
−1.5
−1.0
−0.5
0
0.5
1.0
1.5
−2
−1
1
2
2
4
6
8
100
200
300
400
600
800
1000
2.5
5.0
7.5
10.0
−2.5
−5.0

(a) (b)

(c) (d)

(e) (f)

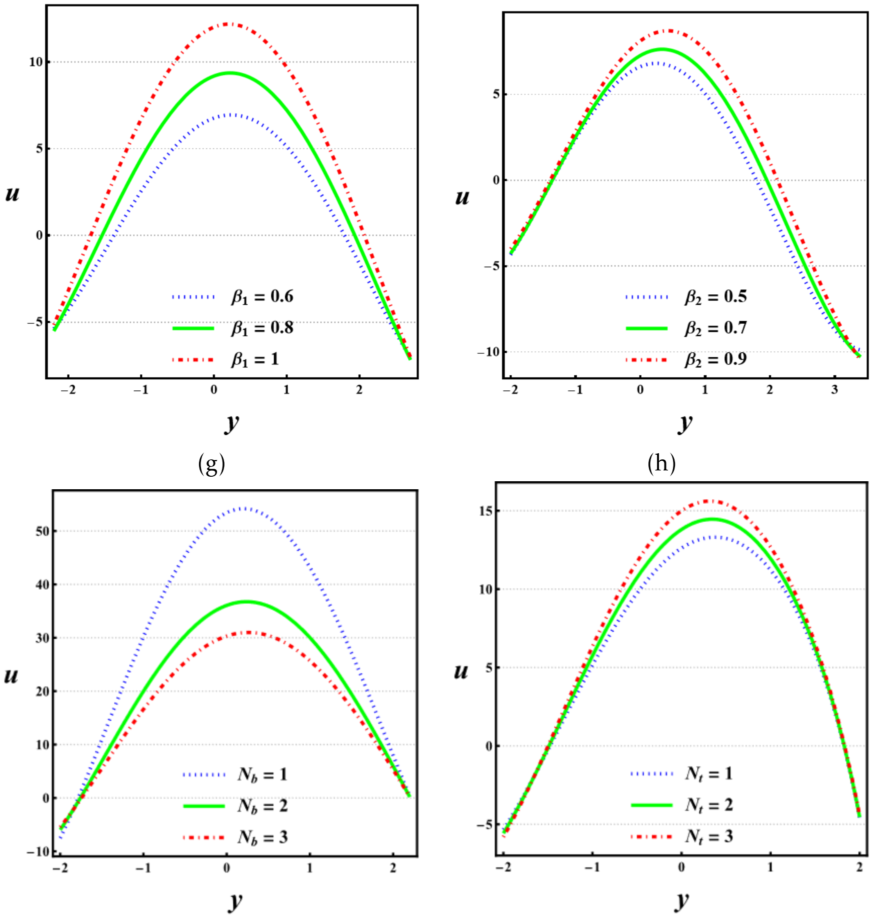

(g) (h)

(i) (j)

FIGURE 3. Influence of various parameters on axial velocity: (a) m_e, (b) U_{hs}, (c) ϕ_2, (d) κ, (e) M, (f) a, (g) β_1, (h) β_2, (i) N_b, and (j) N_t.

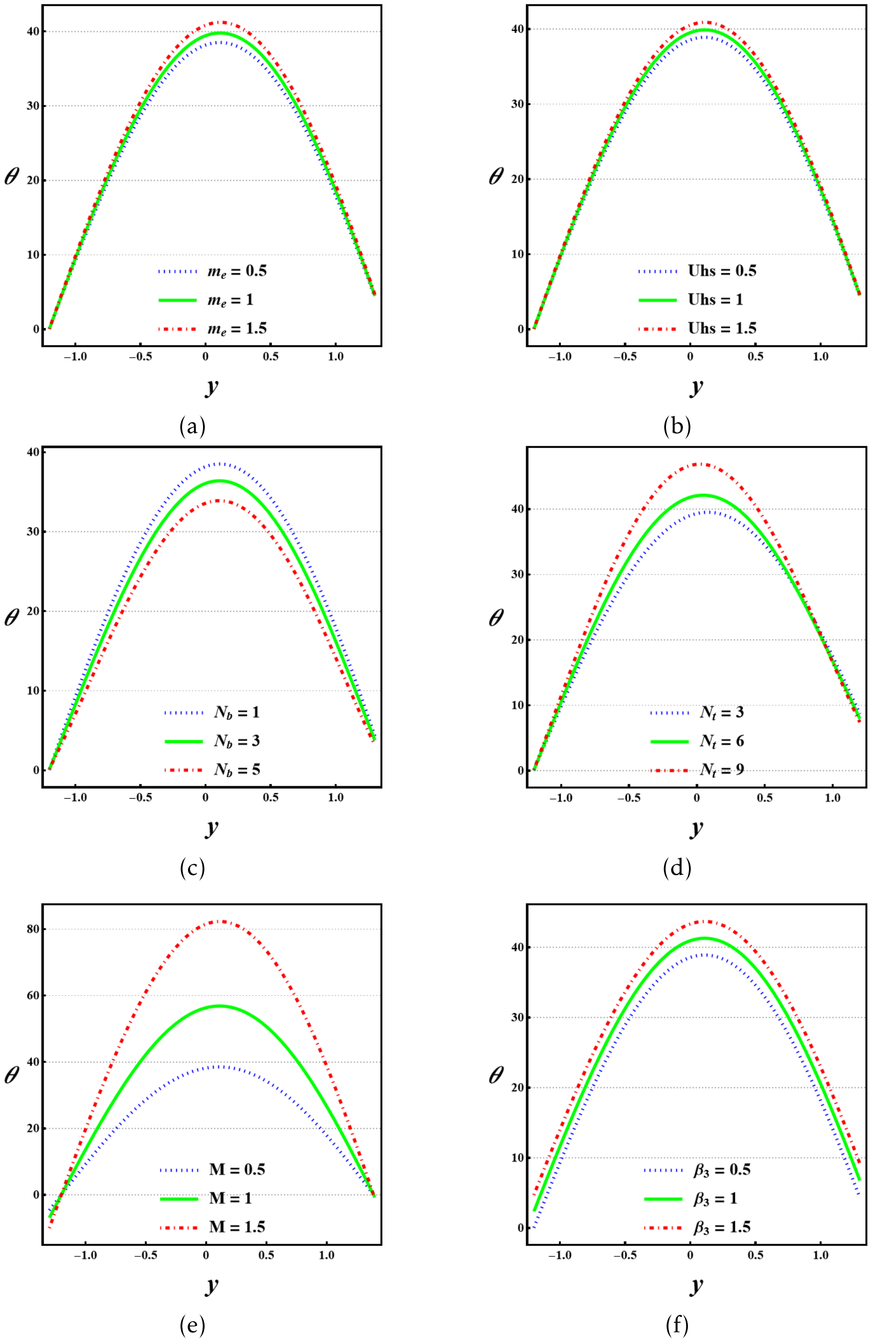

(a) (b)

(c) (d)

(e) (f)

Figure 4. Variation of temperature profile for different values of (a) m_e, (b) U_{hs}, (c) N_b, (d) N_t, (e) M, and (f) β_3.

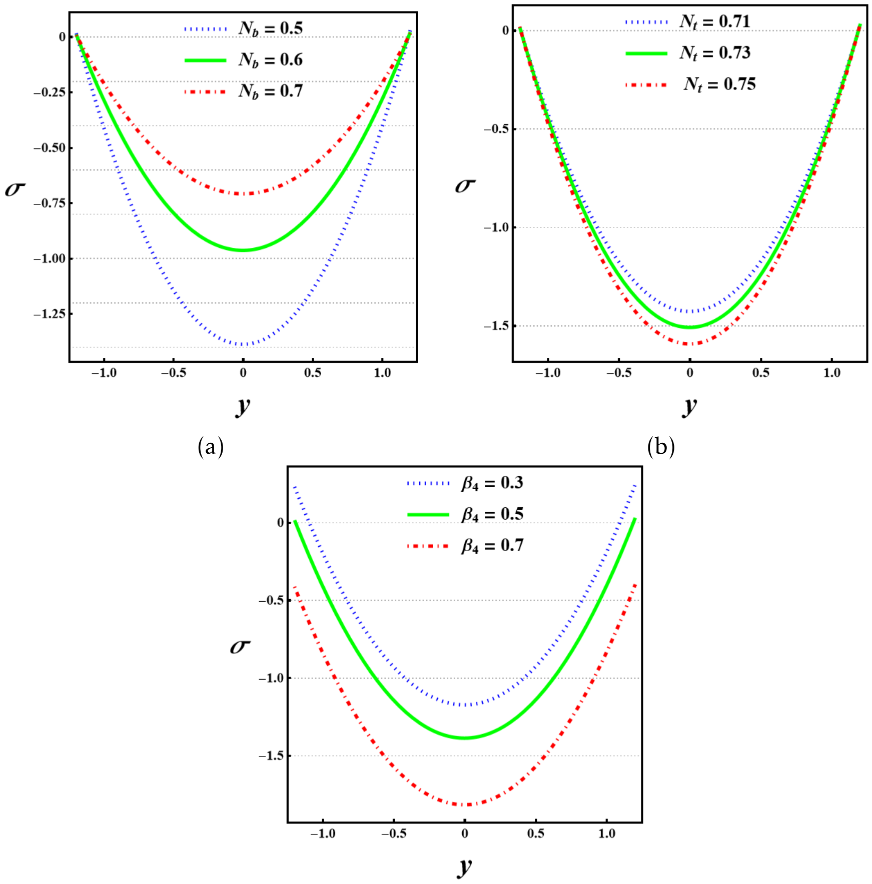

(a) (b)

(c)

FIGURE 5. Variation of concentration profile for different values of (a) N_b, (b) N_t, and (c) β_4 under fixed parameter conditions.

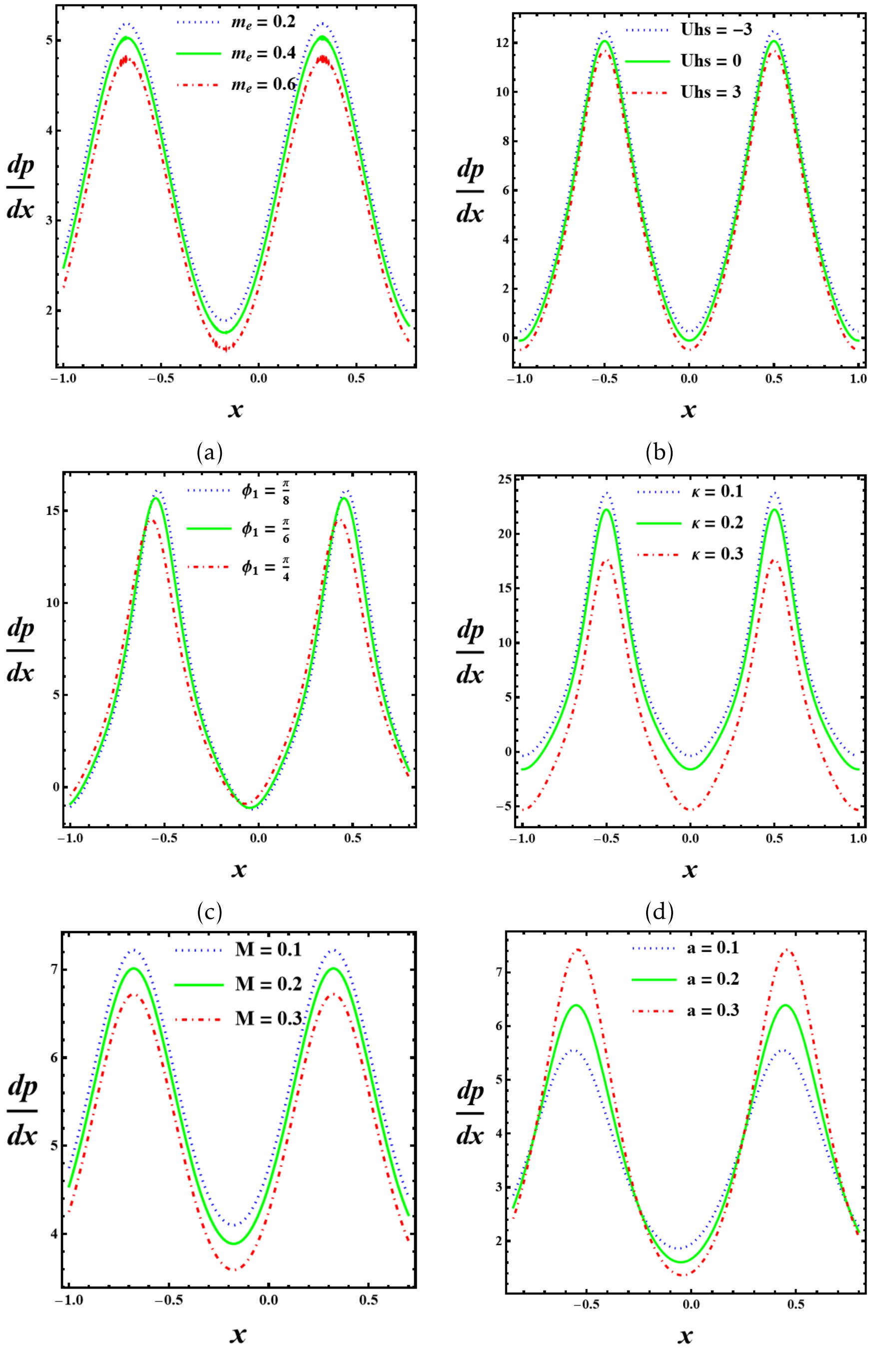
$m_e = 0.2$
$m_e = 0.4$
$m_e = 0.6$
$\frac{dp}{dx}$
x
Uhs = −3
Uhs = 0
Uhs = 3
$\phi_1 = \frac{\pi}{8}$
$\phi_1 = \frac{\pi}{6}$
$\phi_1 = \frac{\pi}{4}$
$\kappa = 0.1$
$\kappa = 0.2$
$\kappa = 0.3$
M = 0.1
M = 0.2
M = 0.3
a = 0.1
a = 0.2
a = 0.3
−1.0
−0.5
0.0
0.5
1.0

(a) (b)

(c) (d)

(e) (f)

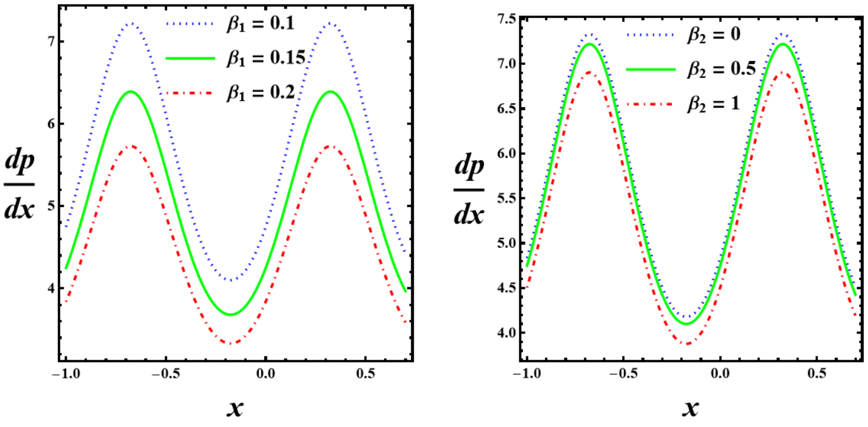

(g) (h)

Figure 6. Pressure gradient along the channel under different physical conditions for various values of (a) m_e, (b) U_{hs}, (c) ϕ_1, (d) κ, (e) M, (f) a, (g) β_1, and (h) β_2.

5. Results and Discussion

In this section, the influence of various physical parameters on the velocity of the flow, temperature, concentration, or other relevant profiles is analyzed through graphical representations. Unless otherwise specified, all parameters are held constant during simulations, and the specific parameter being studied is varied to observe its effect. The fixed values for each parameter are consistent across all cases, while the respective varying values are clearly indicated within the figures themselves for clarity and reference. The graphs are plotted by varying the indicated parameter while keeping all others fixed at the following default values: (a) $m_e = 0.5$, (b) $U_{hs} = 1$, (c) $\phi_2 = 0.0095$, (d) $\kappa = 0.5$, (e) $M = 1$, (f) $a = 0.1$, (g) $\beta_1 = 0.6$, (h) $\beta_2 = 0.2$, (i) $N_b = 0.5$, (j) $N_t = 0.5$, (k) $\beta_3 = 0.6$ (l) $\beta_4 = 0.5$.
Fig. 3 shows the subtle nature of the effect of various physical parameters on the axial velocity profile when subjecting nanofluids to the electroosmotic-driven peristaltic transportation through a vertically oriented porous channel with rough boundaries. The electroosmotic parameter m_e, as seen in Fig. 3a, greatly enhances the velocity of the fluid by increasing the electrokinetic body force, which is created in the electrical double layer. This body force, which is parallel to the channel, acts as an acceleration mechanism in the motion of the bulk nanofluid by offsetting the resistive drag due to viscous forces. Correspondingly, Fig. 3b emphasizes the effect of the Helmholtz - Smoluchowski slip velocity U_{hs}, in which the enhancement of U_{hs} results in a sharp upward curve in the flow velocity. This is attributed to the enhanced electrokinetic activity at the wall-fluid interface, which facilitates momentum transfer and promotes near-wall fluid mobility. In contrast, the effect of roughness is observed in Fig. 3c, where the roughness parameter of the walls ϕ_2 causes a significant reduction in axial velocity. As ϕ_2 increases, the rough nature of the walls destroys the symmetry of

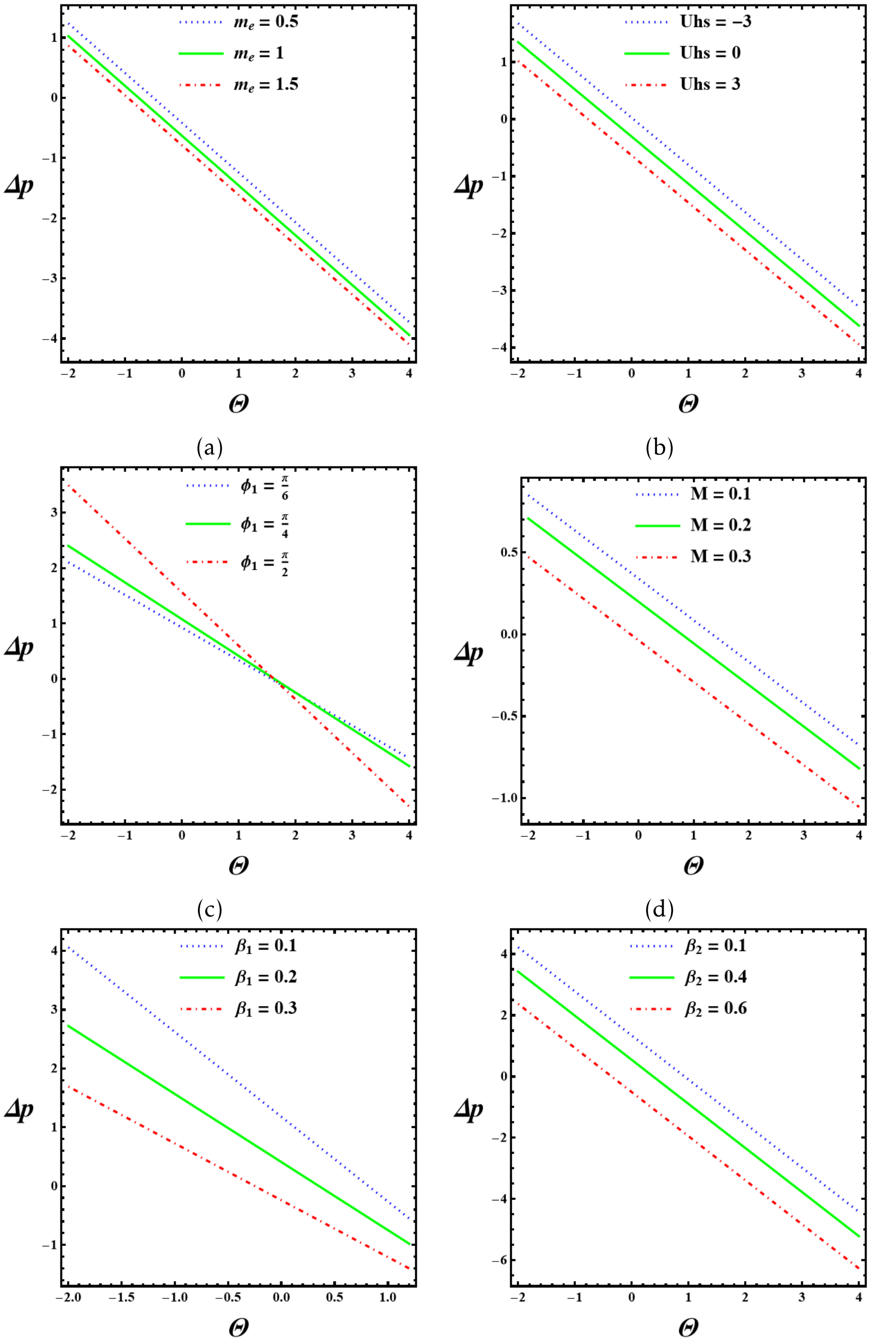

(a) (b)

(c) (d)

(e) (f)

the streamlines and enhances viscous dissipation, thereby inhibiting flow acceleration. The interaction between flow resistance and permeability is observed in Fig. 3d, where increasing values of the porous permeability

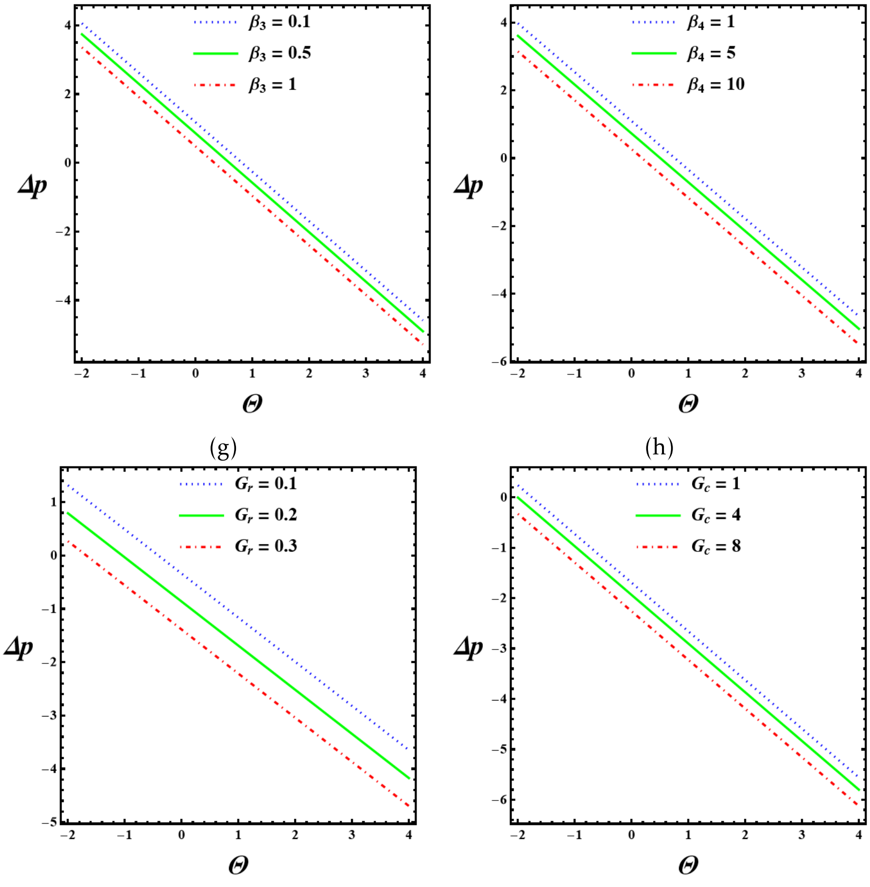

(g) (h)

(i) 7(j)

Figure 7. Variation of pressure gradient Δp for various values of (a) m_e, (b) U_{hs}, (c) ϕ_1, (d) M, (e) β_1, (f) β_2, (g) β_3, (h) β_4, (i) G_r, and (j) G_c.

parameter κ indicate higher velocities. In this case, greater permeability lessens the internal drag effect of the porous matrix, making it easier for the nanofluid to move through the channel. A characteristic magnetic signature is depicted in Fig. 3e, where the Hartmann number M influences the velocity field. A greater magnetic field strength suppresses the velocity due to the Lorentz force, which exerts a resistive damping effect that opposes both the electroosmotic and pressure-driven flows. The amplitude of the peristaltic wave a, presented in Fig. 3f, dynamically adjusts the channel geometry and increases fluid propulsion. A higher amplitude leads to greater wall deformation, thus increasing net flow rates and introducing asymmetry into the velocity profiles. The boundary dynamics governed by slip conditions further affect flow behavior. Figs. 3g and 3h illustrate that first-order (β_1) and second-order (β_2) slip parameters enhance axial

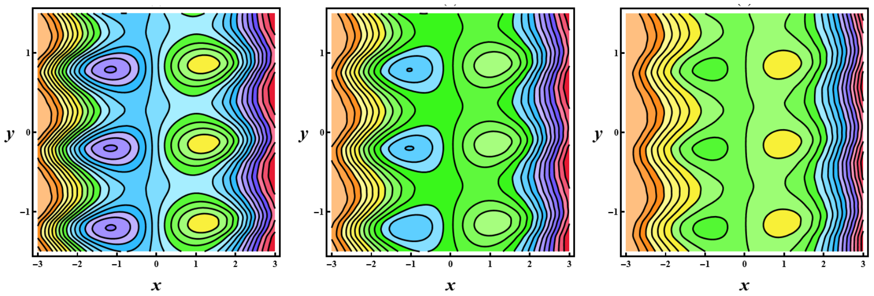

(a) (b) (c)

Figure 8. Streamlines of (a) m_e=0.5, (b) m_e=1, and (c) m_e=1.5.

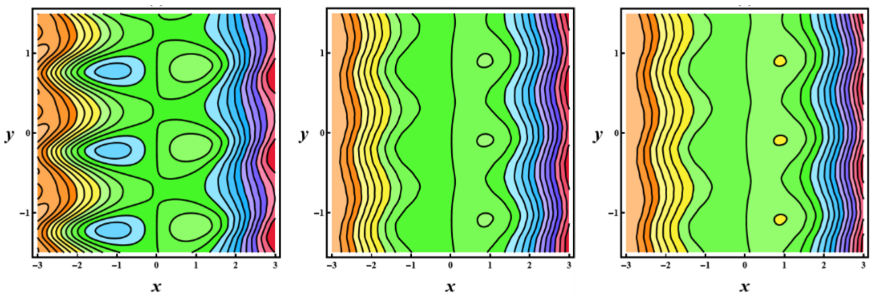

(a) (b) (c)

Figure 9. Streamlines of (a) U_{hs}=-0.5, (b) U_{hs}=0.1, and (c) U_{hs}=0.5.

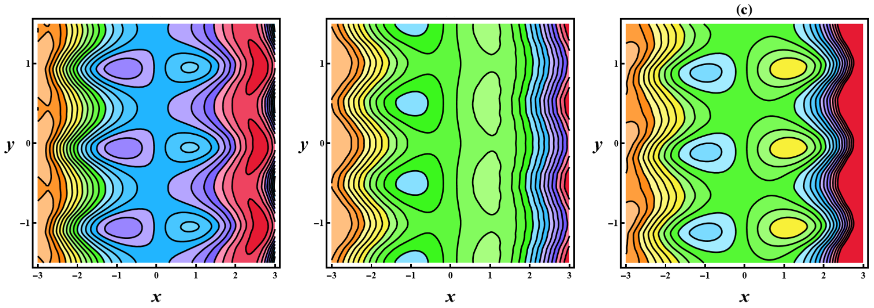

(a) (b) (c)

Figure 10. Streamlines of (a) ϕ_1=$\pi/6$, (b) ϕ_1=$\pi/4$, and (c) ϕ_1=$\pi/3$

velocity. These slip conditions relax the classical no-slip condition and allow partial slip at the walls, which reduces shear stress and allows higher

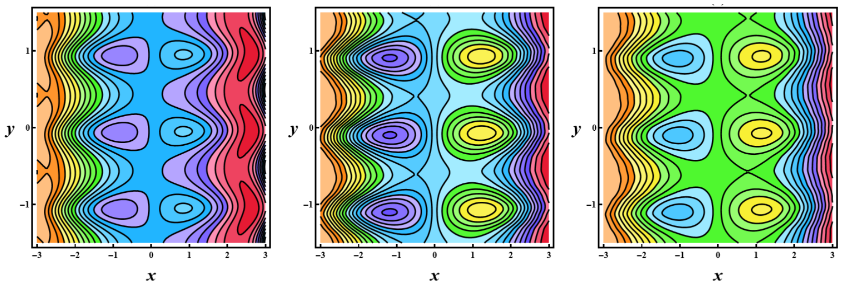

(a) (b) (c)

Figure 11. Streamlines of (a)ϕ_2=0.001, (b) ϕ_2=0.008, and (c) ϕ_2=0.009.

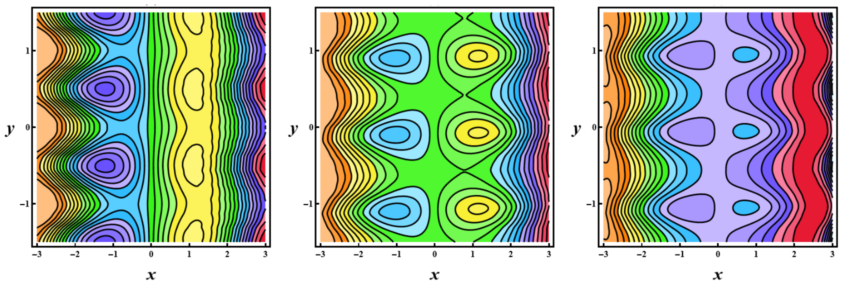

(a) (b) (c)

Figure 12. Streamlines of (a) k=0.5, (b) k=0.5, and (c) k=0.5.

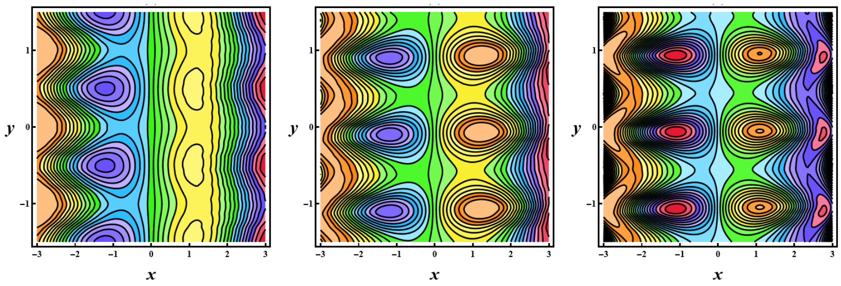

(a) (b) (c)

Figure 13. Streamlines of (a) M=1, (b)M=1.5, and (c) M=2.

flow throughout, especially at micro- and nanoscales where slip effects become significant. The role of nanoparticle transport mechanisms is emphasized in Figs. 3i and 3j. With increasing Brownian motion parameter N_b in Fig. 3i, axial velocity decreases due to increased random motion of nanoparticles, which increases local viscosity and disrupts directed flow, creating a resistive effect on fluid momentum. This microscopic stirring

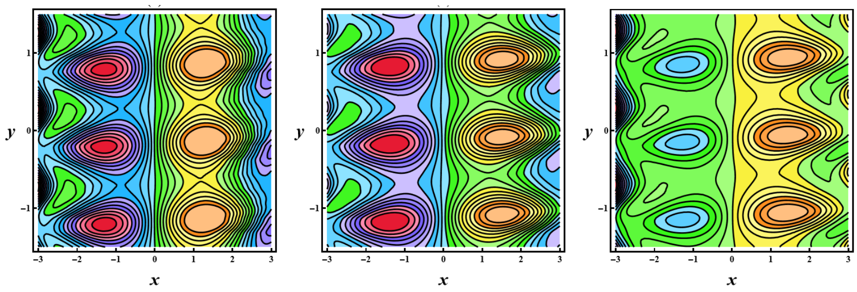

(a) (b) (c)

Figure 14. Streamlines of (a) a=0.1, (b) a=0.2, and (c) a=0.3.

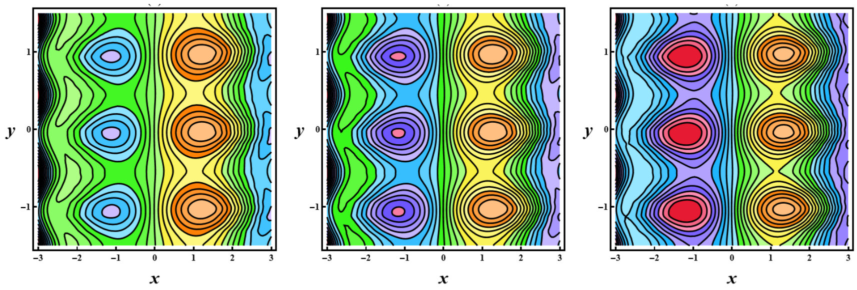

(a) (b) (c)

Figure 15. Streamlines of (a) β_1=0.1, (b) β_1=0.15, (c) and β_1=0.2.

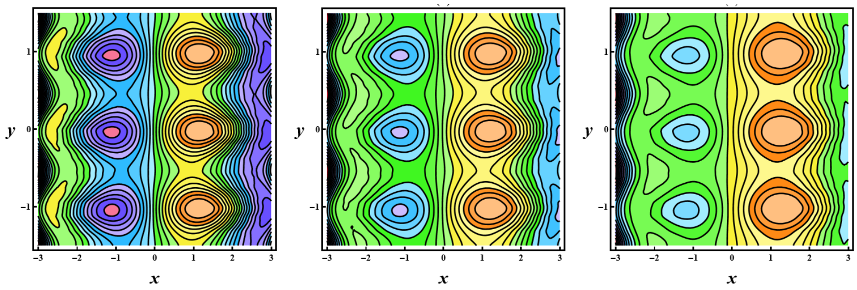

(a) (b) (c)

Figure 16. Streamlines of (a) β_2=0.1, (b) β_2=0.2, (c) and β_1=0.3.

adds internal drag, counteracting the effects of electroosmosis and peristalsis. Conversely, Fig. 3j shows that the velocity increases with higher thermophoresis parameter N_t. The migration of nanoparticles from hot to cold regions due to temperature gradients reduces nanoparticle concentration near the heated wall, thereby decreasing thermal resistance and viscosity in that region. This redistribution enables smoother fluid movement

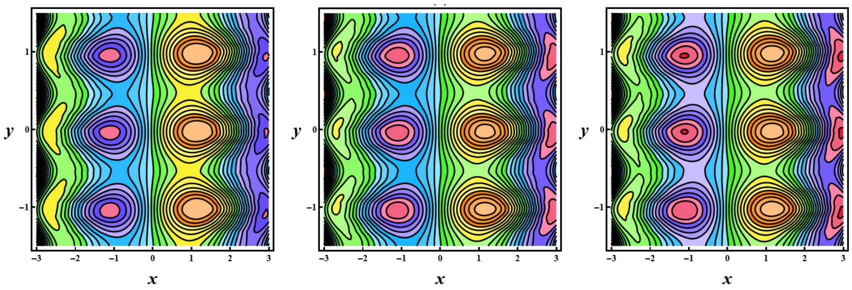

(a) (b) (c)

Figure 17. Streamlines of (a) β_3=0.2, (b) β_3=0.4, (c) and β_3=0.5.

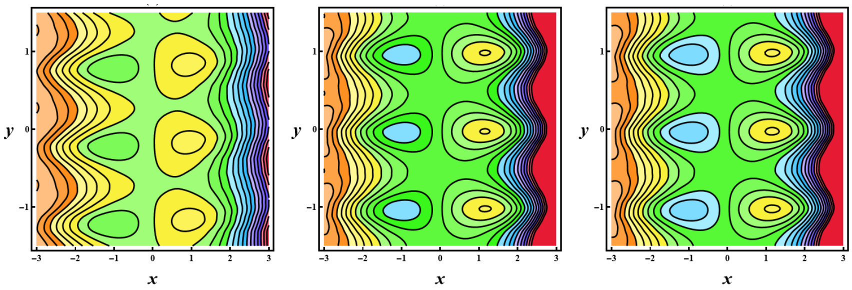

(a) (b) (c)

Figure 18. Streamlines of (a) β_4=0.1, (b) β_4=0.15, (c) and β_4=0.3.

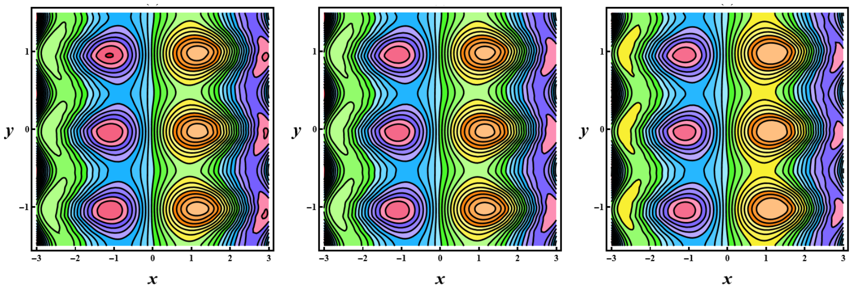

(a) (b) (c)

Figure 19. Streamlines of (a) N_b=0.1, (b) N_b=0.3, and (c) N_b=0.5.

and increases the flow rate. These trends underscore the intricate interplay between nanoparticle transport, electrokinetic forces, and peristaltic pumping in nanofluidic systems under coupled thermal and electrokinetic conditions.

The responses of temperature θ to changes in physical parameters along

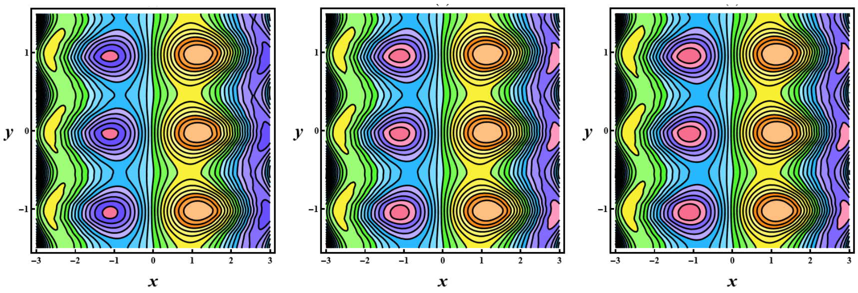

(a) (b) (c)

Figure 20. Streamlines of (a) N_t=0.1, (b) N_t=0.3, and (c) N_t=0.5.

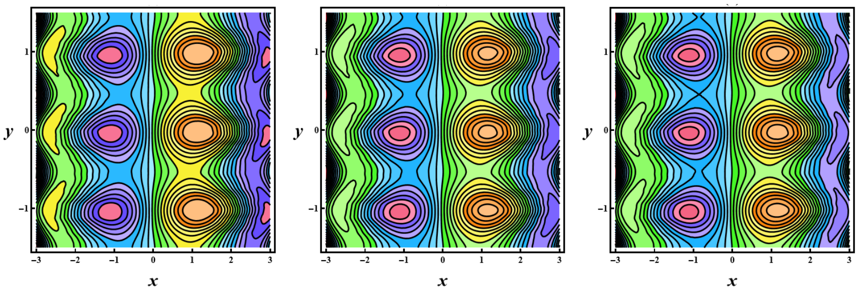

(a) (b) (c)

Figure 21. Streamlines of (a) G_r=1, (b) G_r=3, and (c) G_r=5.

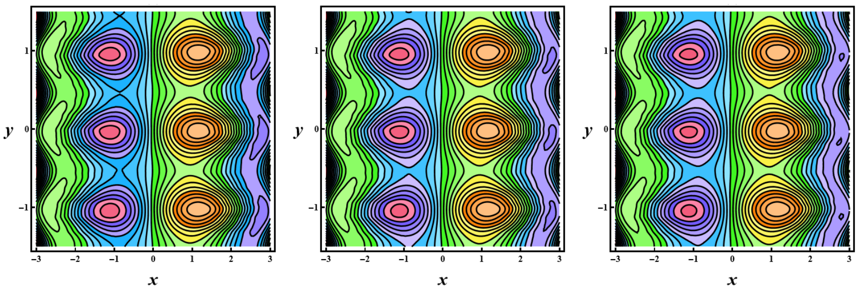

(a) (b) (c)

Figure 22. Streamlines of (a) G_c=0.5, (b) G_c=1, and (c) G_c=1.5.

the y-direction are illustrated in Figs. 4a to 4f. The temperature profile θ rises across the channel when the electroosmotic parameter m_e increases, as shown in Fig. 4a. This indicates that enhanced fluid motion due to electroosmosis leads to increased internal heating. The center of the channel exhibits the highest peak temperature, which becomes more pronounced with higher m_e. The temperature of the channel also increases gradually when the Helmholtz–Smoluchowski velocity U_{hs} increases, as observed in Fig. 4b. This suggests that wall slip intensifies flow-induced heating. With rising U_{hs}, the central temperature peak becomes slightly more evident. Fig. 4c demonstrates the influence of the Brownian motion parameter N_b on temperature θ. The temperature increases with increasing N_b because intensified Brownian motion promotes more uniform nanoparticle dispersion, which mitigates localized heat accumulation and spreads heat more evenly throughout the channel. The effect of the thermophoresis parameter N_t on temperature is shown in Fig. 4d. As N_t increases, the temperature rises due to thermophoretic motion of nanoparticles from hotter to cooler regions, effectively transporting heat and raising the overall temperature. Fig. 4e illustrates the relationship between temperature θ and the magnetic field parameter M. An increase in M results in a higher temperature. This is attributed to the Lorentz force resisting fluid motion, which reduces convective heat removal and increases thermal retention in the fluid. Finally, Fig. 4f shows the influence of the radiation parameter β_3 on temperature. As β_3 increases, the temperature decreases. This is due to enhanced thermal radiation, which allows the fluid to dissipate more energy to the surroundings, thereby lowering the fluid temperature.

Fig. 5 presents the nanoparticle concentration profile variation under the effects of Brownian motion, thermophoresis, and concentration slip effects. In Fig. 5a, a rise in the Brownian motion parameter N_b causes an increase in concentration across the channel. The enhanced random motion of nanoparticles leads to stronger diffusion and facilitates a more even distribution of particles throughout the flow domain. This diffusion-driven mechanism increases particle concentration in the core region, especially away from the boundary layers, resulting in an overall rise in concentration levels. Fig. 5b illustrates that increasing the thermophoresis parameter N_t leads to a noticeable reduction in concentration. Thermophoretic forces drive nanoparticles from hot regions near the boundaries toward cooler regions within the fluid bulk, thus reducing particle density near the heated surfaces. This migration effect decreases the local concentration near boundaries and redistributes particles more broadly, causing a net reduction in average concentration throughout the channel. In Fig. 5c, the concentration decreases as the concentration slip parameter increases. The presence of concentration slip at the wall relaxes the boundary condition on diffusive flux, allowing nanoparticles to escape or bypass the wall rather than adhere to or diffuse into it. As a result, fewer particles accumulate near the wall, leading to a thinner concentration boundary layer and a lower peak concentration in the bulk region. Concentration slip acts as a resistance to nanoparticle accumulation, effectively regulating the efficiency of mass transport within the nanofluidic system.

Fig. 6 shows the variation of the pressure gradient in response to alterations in key flow-controlling factors governing electroosmotic peristaltic nanofluid movement through a porous vertical channel under second-order slip and magnetic effects. An increase in the electroosmotic parameter m_e, as shown in Fig. 6a, results in a clear drop in the pressure gradient since the enhanced electroosmotic body force effectively drives the fluid forward, reducing the need for a high pressure to maintain motion. In Fig. 6b, a similar trend is observed for the Helmholtz–Smoluchowski velocity U_{hs}, where increasing U_{hs} intensifies electrokinetic slip at the wall-fluid interface, thereby lowering viscous resistance and decreasing the required pressure gradient. Fig. 6c illustrates the role of the phase difference ϕ_1 between upper and lower peristaltic waves. Increasing ϕ_1 introduces asymmetry in wall motion, causing geometric skewness and irregularities in flow. This leads to alternating zones of flow constriction and expansion, which increase resistance and elevate the pressure gradient. The influence of permeability κ is shown in Fig. 6d, where an increase in κ results in a lower pressure gradient due to reduced internal resistance, allowing easier fluid penetration through the porous medium. In contrast, Fig. 6e shows that the Hartmann number M causes an increase in the pressure gradient. The Lorentz force generated by the magnetic field opposes the flow, requiring greater pressure to maintain steady transport, especially in an electrically conducting nanofluid. The geometric parameter of wave amplitude a, depicted in Fig. 6f, shows that higher values of a lead to stronger wall-induced compression and expansion. This increases internal resistance and causes greater flow reversal, thereby increasing the pressure gradient. Figs. 6g and 6h explore the impact of the velocity slip parameters β_1 and β_2. As seen in Fig. 6g, increasing the first-order slip parameter β_1 reduces frictional drag at the boundary, lowering the pressure gradient. Similarly, Fig. 6h demonstrates that an increase in second-order slip β_2 further decreases near-wall resistance by introducing curvature-dependent behavior and enhancing slip, resulting in a reduced pressure gradient. In summary, while stronger electroosmotic forces, higher Helmholtz velocity, greater permeability, and enhanced wall slip help reduce the pressure gradient, increases in magnetic field strength, wave amplitude, and phase difference tend to elevate it.

The significance of different physical parameters lies in how they affect the pressure rise and control the overall flow behaviour in the system. Fig. 7a and Fig. 7b show that stronger electroosmotic effects reduce the pressure rise, making the flow easier. Fig. 7c and Fig. 7d demonstrate how changes in the different physical parameters (ϕ_1, M) affect the pressure rise. As ϕ_1 increases, the pressure rise decreases, and as M increases, the pressure rise increases. Figs. 7e–7h, show that, as the effects of the parameters β_1, β_2, β_3, and β_4 increase, the pressure rise decreases. 7i and Fig. 7j indicate that decreasing the pressure rise by increasing G_r or G_c allows flow under buoyancy and concentration effects.

To illustrate the flow behavior within the channel, streamline patterns are drawn for different physical parameters, which highlight the effect on flow structure and at circulation zones. As the electroosmotic parameter m_e increases (see Fig. 8), the bolus size and streamline density decrease, showing that stronger electric forcing promotes plug-like flow and reduces trapping regions. As the Helmholtz-Smoluchowski velocity U_{hs} increases (see Fig. 9), bolus size decreases and streamline density increases, reflecting faster wall-driven flow that flattens the bolus and enhances flow uniformity. As the phase difference ϕ_1 increases (see Fig. 10), the bolus size increases and streamlines become more asymmetric and dense, indicating stronger peristaltic wall interaction that enhances fluid trapping and alters flow symmetry. With increasing wall roughness (ϕ_2) (see Fig. 19), bolus size enlarges and streamlines become irregular, reflecting enhanced flow resistance and stronger fluid trapping due to surface disturbance. As the Darcy permeability κ increases (see Fig. 12), the bolus size decreases and streamlines become denser, indicating that increased permeability allows easier flow and reduces fluid entrapment. As the magnetic field parameter (Hartmann number) M increases (see Fig. 13), the bolus size increases and streamlines become more confined, due to the Lorentz force resisting fluid motion and enhancing fluid retention. As the amplitude of the peristaltic wave a increases (see Fig. 14), the bolus size increases and streamlines thicken, due to greater wall compression and stronger fluid trapping. As the slip velocity parameters β_1, β_2, and thermal (β_3) and concentration (β_4) slip increase (see Fig. 15–Fig. 18), the bolus size decreases and streamlines become more flattened, indicating reduced wall resistance and weaker fluid trapping due to enhanced slip at the boundaries. As the Brownian motion parameter N_b (see Fig. 19) increases, the streamlines are more dispersed, which represents increased nanoparticle diffusion and internal mixing. This results in higher disturbance in the flow field and encourages secondary flow structures. As the thermophoresis parameter N_t increases (see Fig. 20), the bolus size decreases and streamlines thin out, since strong thermophoretic force disrupts trapping by moving particles from hot to cold regions.As the Grashof number G_r increases (see Fig. 21), the bolus size increases and streamlines become more circulatory, indicating enhanced buoyancy-driven flow that strengthens fluid trapping and recirculation. Increasing the local Grashof number G_c (see Fig. 22) leads to a noticeable increase in bolus size and streamline density, reflecting the enhanced influence of concentration-induced buoyancy forces that promote stronger fluid entrapment.

6. Conclusion

This research provides an in-depth semi-analytical study of the electroosmotic-driven peristaltic movement of nanofluids in a vertical porous channel with rough walls, considering the effects of a magnetic field and second-order slip boundary conditions. A key feature of this study is the integration of four essential microfluidic phenomena electroosmosis, magnetohydrodynamics, porous drag, and higher-order slip into a unified framework, addressing a notable gap in current literature. The governing nonlinear equations were addressed using the Homotopy Perturbation Method (HPM), revealing how various physical parameters influence fluid velocity, temperature, nanoparticle concentration, pressure distribution, and streamline behavior. The findings indicate that

- Electroosmotic forces significantly improve flow rates while decreasing pressure needs and fluid transport.
- Wall roughness and magnetic field strength create flow resistance and elevate pressure gradients.

- Porous permeability aids in smoother flow and reduces pressure accumulation.
- Second-order velocity and thermal slip lessen wall resistance, enhancing transport efficiency.
- Nanoparticle behavior, affected by Brownian motion and thermophoresis, plays a dual role in regulating thermal and mass transport.

Overall, the results suggest that careful adjustment of these parameters can enhance the performance of microfluidic systems. This research provides important theoretical insights for the development of advanced micro- and nanofluidic devices, such as lab-on-chip systems, biomedical transport applications, and drug delivery technologies, where precise flow management and energy efficiency are essential.

Table 1. List of symbols and their physical meanings

Symbol	**Description**	**Unit**
ρ_P	Density of the fluid at constant pressure	kg/m^3
T_1, T_0	Temperature at the wall	K
C_0, C_1	Concentration at the wall	mol/m^3
T	Temperature of the fluid	K
C	Concentration of the fluid	mol/m^3
C_p	Specific heat	J/(kg·K)
C_f	Specific heat of the nanofluid	J/(kg·K)
μ_f	Viscosity of the nanofluid	Pa·s
k	Thermal diffusivity	W/(m·K)
D_B	Brownian motion coefficient	m^2/s
D_T	Thermophoretic diffusion coefficient	m^2/s
δ	Wave number	m^{-1}
u, v	Velocity components in wave frame	m/s
Re	Reynolds number	–
ϑ_f	Kinematic viscosity	m^2/s
N_b	Brownian motion parameter	–
N_t	Thermophoresis parameter	–
θ	Temperature distribution	–
σ	Concentration distribution	–
M	Hartmann number	–
U_{hs}	Helmholtz-Smoluchowski velocity	m/s
$\bar{E}$	Electrical potential	V
G_r	Local temperature Grashof number	–
G_c	Local nanoparticle Grashof number	–
τ	Effective heat capacity	$J/(m^3 \cdot K)$
β_1, β_2	First and second order velocity slip	–
β_3	First order thermal slip	–
β_4	First order concentration slip	–
Q, q	Fixed and wave frame flow rate	m^3/s
Θ	Dimensionless flow rate	–
ϕ_1	Phase difference	rad
ϕ_2	Roughness parameter	–
$\bar{U}, \bar{V}$	Velocity components in fixed frame	m/s
H_1, H_2	Height of the channel	m
d_1, d_2	Width of the channel	m
a_1, a_2	Amplitude of the wave	m
b_1	Height surface roughness	m
c	Wave speed	m/s
$\bar{t}$	Time in fixed frame	s
λ	Wavelength	m
λ_1	Pitch	m
ρ_f	Nanofluid density	kg/m^3
$\bar{P}$	Pressure in fixed frame	Pa
k_1	Permeability	m^2
σ_e	Electrical conductivity	S/m
B_0	Intensity of external magnetic field	T
ρ_e	Net charge density	C/m^3
g	Acceleration due to gravity	m/s^2

References

[1] R. Ahmed, N. Ali, K. Al-Khaled, S. U. Khan, I. Tlili, Finite difference simulations for non-isothermal hydromagnetic peristaltic flow of a bio-fluid in a curved channel: applications to physiological systems, *Comput. Methods Programs Biomed.*, **195** (2020) 105672.

[2] W. A. Khan, S. Farooq, S. Kadry, M. Hanif, F. J. Iftikhar, S. Z. Abbas, Variable characteristics of viscosity and thermal conductivity in peristalsis of magneto-Carreau nanoliquid with heat transfer irreversibilities, *Comput. Methods Programs Biomed.*, **190** (2020) 105355.

[3] C. Pozrikidis, A study of peristaltic flow, *J. Fluid Mech.*, **180** (1987) 515–527.

[4] K. Guedri, M. M. Lashin, A. Abbasi, S. U. Khan, W. Farooq, M. I. Khan, A. M. Galal, Biomedical and engineering aspects of nonlinear radiative peristaltic transport in chemically reactive blood flow of Ellis nanofluid in an asymmetric channel with activation energy, *Chin. J. Phys.*, **83** (2023) 650–663.

[5] P. Sanil, M. Gudekote, R. Choudhari, H. Vaidya, K. V. Prasad, Heat transfer analysis on peristaltic transport of Sisko fluid in an inclined uniform channel, *J. Adv. Res. Fluid Mech. Therm. Sci.*, **103**(2) (2023) 157–179.

[6] K. Connington, Q. Kang, H. Viswanathan, A. Abdel-Fattah, S. Chen, Peristaltic particle transport using the lattice Boltzmann method, *Phys. Fluids*, **21**(5) (2009).

[7] W. Mahmood, M. Sajid, M. N. Sadiq, N. Ali, K. Ullah, Influences of lubrication on asymmetric peristaltic movement and its bifurcation, *Int. J. Mod. Phys. B*, **38**(02) (2024) 2450018.

[8] R. Ibanez, M. Shokrian, J. H. Nam, D. H. Kelley, Simple analytic model for peristaltic flow and mixing, *Phys. Rev. Fluids*, **6**(10) (2021) 103101.

[9] R. Choudhari, H. Vaidya, S. Alshehery, D. Tripathi, I. Khan, N. F. M. Noor, A. Patil, Heat transfer in peristaltic flow of electrokinetically modulated Carreau fluid under the influence of magnetic field, *ZAMM–J. Appl. Math. Mech.*, **105**(3) (2025) e202300997.

[10] I. Fatima, S. Asghar, Imposed pressure driven flow in peristalsis, *Adv. Mech. Eng.*, **12**(11) (2020) 1687814020971063.

[11] S. Farooq, T. Shoaib, S. Z. B. Bukhari, A. S. Alqahtani, M. Y. Malik, S. Abdullaev, S. E. Alhazmi, Peristaltic motion of Jeffrey fluid with nonlinear mixed convection, *Heliyon*, **9**(11) (2023).

[12] M. Masuduzzaman, C. Bakli, M. Barisik, B. Kim, Applied electric field effects on diffusivity and electrical double-layer thickness, *Small*, **20**(46) (2024) 2404397.

[13] A. Alizadeh, W. L. Hsu, M. Wang, H. Daiguji, Electroosmotic flow: From microfluidics to nanofluidics, *Electrophoresis*, **42**(7–8) (2021) 834–868.

[14] T. D. Mai, C. Lee, J. Ryu, Numerical study of rectified electroosmotic flow in nanofluidics: Influence of surface charge and geometrical asymmetry, *Phys. Fluids*, **35**(9) (2023).

[15] W. Qian, K. Doi, S. Kawano, Effects of polymer length and salt concentration on the transport of ssDNA in nanofluidic channels, *Biophys. J.*, **112**(5) (2017) 838–849.

[16] V. Sridhar, N. S. Khashi'ie, K. Ramesh, Thermal and electroosmotic transport of blood-copper/platinum nanofluid in a microfluidic vessel with entropy analysis, *Proc. Inst. Mech. Eng. Part E J. Process Mech. Eng.*, **238**(5) (2024) 2360–2375.

[17] S. Sarkar, S. Ganguly, Fully developed thermal transport in combined pressure and electroosmotically driven flow of nanofluid in a microchannel under the effect of a magnetic field, *Microfluid. Nanofluid.*, **18**(4) (2015) 623–636.

[18] A. Kumar, D. Tripathi, A. K. Tiwari, P. Seshaiyer, Magnetic field modulation of electroosmotic-peristaltic flow in tumor microenvironment, *Phys. Fluids*, **37**(4) (2025).

[19] A. Riaz, M. D. Nawaz, M. N. Aslam, S. U. Khan, S. ur Rehman, G. Alhamzi, Effect of boundary slips and magnetohydrodynamics on peristaltic mechanism of Jeffrey nanofluid along with microorganisms through a porous medium, *Heliyon*, **10**(13) (2024).

[20] M. Reza, A. Rana, Thermo-fluidic transport of electromagnetohydrodynamic flow of sodium alginate based Casson nano fluid passing through a porous microtube under the effect of streaming potential, *Int. J. Eng. Technol.*, **10**(1) (2021) 38–45.

[21] M. Y. Abouzeid, A. A. Shaaban, Electroosmotic flow of micropolar nanofluid through a non-Darcy porous media with von Neumann stability condition, *Special Topics Rev. Porous Media*, **16**(1) (2024) 21–38.

[22] S. Srinivas, R. Gayathri, Peristaltic transport of a Newtonian fluid in a vertical asymmetric channel with heat transfer and porous medium, *Appl. Math. Comput.*, **215**(1) (2009) 185–196.

[23] M. Wang, Q. Kang, Electrokinetic transport in microchannels with random roughness, *Anal. Chem.*, **81**(8) (2009) 2953–2961.

[24] H. Vaidya, F. Mebarek-Oudina, R. Kumar, C. Rajashekhar, K. V. Prasad, S. Kalal, K. S. Nisar, Magnetohydrodynamic Peristaltic Propulsion of Casson Nanofluids with Slip Effects Over Heterogeneous Rough Channel, *Eng. Rep.*, **7**(1) (2025) e13062.

[25] B. Kundu, S. Saha, Review and analysis of electro-magnetohydrodynamic flow and heat transport in microchannels, *Energies*, **15**(19) (2022) 7017.

[26] J. H. He, Homotopy perturbation method: a new nonlinear analytical technique, *Appl. Math. Comput.*, **135**(1) (2003) 73–79.

[27] R. Shukla, A. Kumar, A. Medhavi, D. Tripathi, Heat transfer and surface roughness analysis via peristaltic pumping of viscous fluids through diverging tube, *Numer. Heat Transf. A Appl.*, (2024) 1–21.

[28] H. Vaidya, K. V. Prasad, R. V. Choudhari, D. Tripathi, M. Naganur, Surface roughness impact on bioinspired rhythmic contractile microfluidic membrane pumping mechanism: A computational analysis, *Phys. Fluids*, **37**(6) (2025).

[29] A. Kumar, A. Bhardwaj, D. Tripathi, Thermal analysis in peristaltic pumping: Effects of surface roughness and channel geometries, *Phys. Fluids*, **37**(2) (2025).

[30] A. Pandey, A. Kumar, D. Tripathi, K. Sharma, Membrane-driven flow and heat transfer of viscoelastic fluids: MHD and entropy generation analysis, *Int. J. Numer. Methods Heat Fluid Flow*, (2025).

[1]DEPARTMENT OF MATHEMATICS, MANIPAL INSTITUTE OF TECHNOLOGY BENGALURU, MANIPAL ACADEMY OF HIGHER EDUCATION, MANIPAL, KARNATAKA, INDIA
Email address: `bhavanagadad393@gmail.com`

[1]DEPARTMENT OF MATHEMATICS, MANIPAL INSTITUTE OF TECHNOLOGY BENGALURU, MANIPAL ACADEMY OF HIGHER EDUCATION, MANIPAL, KARNATAKA, INDIA
Email address: `Shetty.jyoti@manipal.edu`

[1]DEPARTMENT OF MATHEMATICS, MANIPAL INSTITUTE OF TECHNOLOGY BENGALURU, MANIPAL ACADEMY OF HIGHER EDUCATION, MANIPAL, KARNATAKA, INDIA
Email address: `rv.choudhari@manipal.edu`

[2]DEPARTMENT OF MATHEMATICS, VIJAYANAGAR SRI KRISHNADEVARAYA UNIVERSITY BALLARY
Email address: `hanumeshvaidya@gmail.com`

[3]DEPARTMENT OF MATHEMATICS, MANIPAL INSTITUTE OF TECHNOLOGY, MANIPAL ACADEMY OF HIGHER EDUCATION, MANIPAL, KARNATAKA, INDIA
Email address: `bs.hadimani@manipal.edu`

[2]DEPARTMENT OF MATHEMATICS, VIJAYANAGAR SRI KRISHNADEVARAYA UNIVERSITY BALLARY
Email address: `prasadkv2007@gmail.com`